



## Resolved Structure of the Arp 220 Nuclei at $\lambda \approx 3$ mm

Kazushi Sakamoto<sup>1</sup>, Susanne Aalto<sup>2</sup>, Loreto Barcos-Muñoz<sup>3,4</sup>, Francesco Costagliola<sup>2</sup>, Aaron S. Evans<sup>4,5</sup>,  
Nanase Harada<sup>1</sup>, Sergio Martín<sup>3,6</sup>, Martina Wiedner<sup>7</sup>, and David Wilner<sup>8</sup>

<sup>1</sup> Academia Sinica, Institute of Astronomy and Astrophysics, Taipei 10617, Taiwan; [ksakamoto@asiaa.sinica.edu.tw](mailto:ksakamoto@asiaa.sinica.edu.tw)

<sup>2</sup> Department of Earth and Space Sciences, Chalmers University of Technology, Onsala Observatory, 439 92 Onsala, Sweden

<sup>3</sup> Joint ALMA Observatory, Alonso de Córdova 3107, Vitacura, Santiago, Chile

<sup>4</sup> National Radio Astronomy Observatory, 520 Edgemont Road, Charlottesville, VA 22903, USA

<sup>5</sup> Department of Astronomy, University of Virginia, P.O. Box 400325, Charlottesville, VA 22904, USA

<sup>6</sup> European Southern Observatory, Alonso de Córdova 3107, Vitacura, Santiago, Chile

<sup>7</sup> LERMA, Observatoire de Paris, PSL Research University, CNRS, Sorbonne Universités, UPMC Univ. Paris 06, F-75014 Paris, France

<sup>8</sup> Harvard-Smithsonian Center for Astrophysics, 60 Garden Street, Cambridge, MA 02138, USA

Received 2017 August 7; revised 2017 September 22; accepted 2017 September 24; published 2017 October 25

### Abstract

We analyze the 3 mm emission of the ultraluminous infrared galaxy Arp 220 for the spatially resolved structure and the spectral properties of the merger nuclei. ALMA archival data at  $\sim 0''.05$  resolution are used for extensive visibility fitting and deep imaging of the continuum emission. The data are fitted well by two concentric components for each nucleus, such as two Gaussians or one Gaussian plus one exponential disk. The larger components in the individual nuclei are similar in shape and extent,  $\sim 100$ – $150$  pc, to the centimeter wave emission due to supernovae. They are therefore identified with the known starburst nuclear disks. The smaller components in both nuclei have about a few 10 pc sizes and peak brightness temperatures ( $T_b$ ) more than twice higher than those in previous single-Gaussian fitting. They correspond to the dust emission that we find centrally concentrated in both nuclei by subtracting the plasma emission measured at 33 GHz. The dust emission in the western nucleus is found to have a peak  $T_b \approx 530$  K and an FWHM of about 20 pc. This component is estimated to have a bolometric luminosity on the order of  $10^{12.5} L_\odot$  and a 20 pc scale luminosity surface density  $10^{15.5} L_\odot \text{ kpc}^{-2}$ . A luminous active galactic nucleus is a plausible energy source for these high values while other explanations remain to be explored. Our continuum image also reveals a third structural component of the western nucleus—a pair of faint spurs perpendicular to the disk major axis. We attribute it to a bipolar outflow from the highly inclined ( $i \approx 60^\circ$ ) western nuclear disk.

**Key words:** galaxies: active – galaxies: individual (Arp 220) – galaxies: ISM – galaxies: nuclei

**Supporting material:** data behind figure

### 1. Introduction

The nearest ultraluminous infrared galaxy Arp 220 has been a key object in our study of the luminous phase in galaxy evolution after a major merger (Sanders & Mirabel 1996; Hopkins et al. 2008). It has two merger nuclei separated by about  $1''$  ( $\sim 400$  pc) on the sky (Scoville et al. 1998; Genzel et al. 2001), each having a  $\sim 100$  pc scale rotating disk of molecular gas (Sakamoto et al. 1999). Vigorous star formation is evident in the nuclei from radio emission due to supernovae (Smith et al. 1998; Barcos-Muñoz et al. 2015, hereafter BM15). Molecular outflows from the individual nuclei have been found (Sakamoto et al. 2009), as is often the case for luminous galactic nuclei (e.g., Ciccone et al. 2014; Sakamoto et al. 2014). Arp 220 is therefore undergoing the merger-driven rapid evolution of galaxy nuclei. Important open issues about the galaxy include the gas flows to, from, and within the two merger nuclei and the structure, physical and chemical properties, and the dominant luminosity sources of the nuclei. On the last point, although nuclear starburst is evident, whether there are any active galactic nuclei (AGNs) with significant luminosities is still under intense study (Paggi et al. 2017; Yoast-Hull et al. 2017, and references therein), mainly because the nuclei are extremely obscured ( $N_H \geq 10^{25}$ – $10^{26} \text{ cm}^{-2}$ , Sakamoto et al. 2008; Wilson et al. 2014; Martín et al. 2016; Scoville et al. 2017, hereafter S17). High-resolution observations at centimeter to submillimeter wavelengths are especially

useful for many of the open issues, thanks to the lower dust opacity there than at shorter wavelengths.

We recently found from our 1 and 0.8 mm observations of Arp 220 with the Atacama Large Millimeter-submillimeter Array (ALMA) that the individual merger nuclei have a composite structure (K. Sakamoto et al. 2017, in preparation). Each nucleus consists of a central compact core and a more extended structure that can together be fitted with two Gaussians. The single-Gaussian models that had been used before are no longer adequate for high-quality data at  $\lesssim 0''.2$  resolution. The central core components have sizes as small as  $0''.1$ – $0''.05$  in FWHM and have higher peak brightness temperatures than estimated with single-Gaussian fits. They are of great interest for unveiling the unknown nature of the luminosity source and for tracing the evolution of the merger nuclei. We therefore extended our structural analysis of the Arp 220 nuclei to ALMA archival data obtained at around 3 mm at  $\sim 0''.05$  resolution. We also decomposed the 3 mm continuum into plasma and dust emission and mapped the dust emission in the individual nuclei. This paper reports the results.

We will refer to the eastern nucleus of Arp 220 as Arp 220 E (sometimes just “E” for short) and to the western nucleus as Arp 220 W (or just “W”). All features within about  $0''.5$  of the centroid of each nucleus will be referred to in this way. We adopt an angular size distance of  $D_A = 85.0$  Mpc ( $1'' = 412$  pc), luminosity distance  $D_L = 87.9$  Mpc, and a

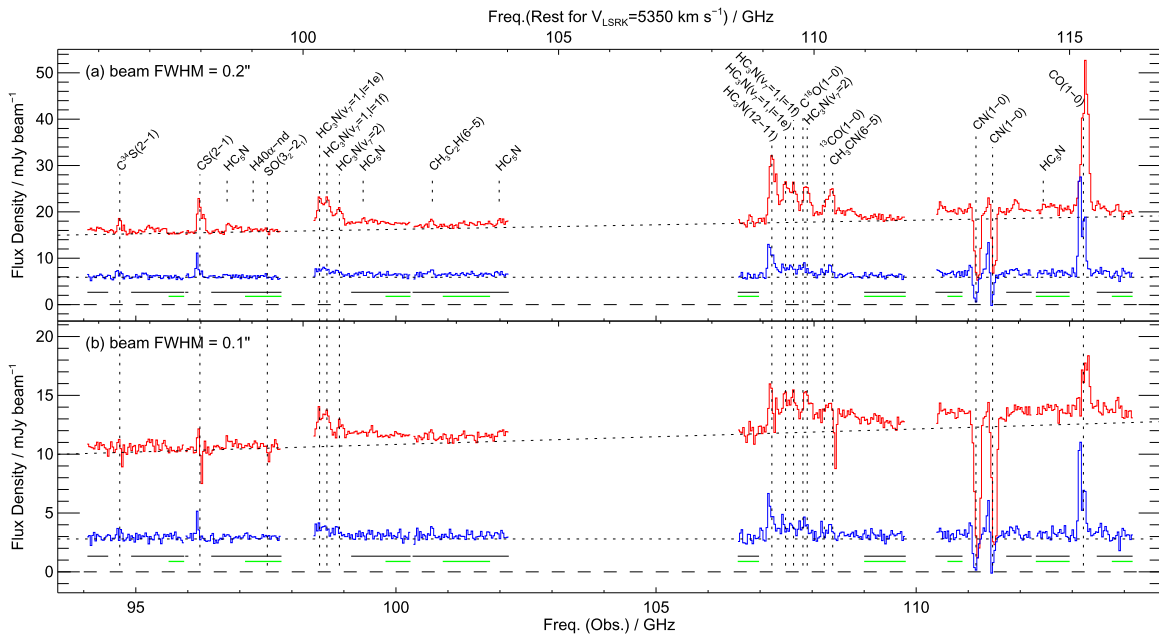


**Figure 1.** Spectra of the Arp 220 nuclei around 100 GHz sampled at the western (red) and eastern (blue) nuclei. Data imaged every 10 MHz were binned to 30 MHz and convolved from about  $0''.09$  resolution to (a)  $0''.2$  and (b)  $0''.1$ . Major lines are labeled with long vertical dotted lines. Some minor lines are also labeled with short vertical lines. The estimated power-law continuum is plotted for each nucleus as a black dotted line. Its power-law (i.e., spectral) index is  $+1.2$  and  $0.0$  for the western and eastern nuclei, respectively, in both panels. The horizontal black and green bars below the spectra indicate the spectral segments that we analyzed as continuum-dominated channels. The black ones are used for continuum imaging and green for visibility fitting.

total IR luminosity of  $L_{8-1000 \mu\text{m}} = 10^{12.28} L_{\odot}$  for the galaxy (Armus et al. 2009) to be consistent with S17.

## 2. ALMA Data

We analyzed archival data of ALMA project 2015.1.00113.S (P.I. Scoville). S17 already reported the part of the project concerning the  $^{12}\text{CO}(1-0)$  line and continuum imaging as well as the spatial and spectral modeling of the CO emission. The data set consists of two tunings around 100 GHz consecutively observed on 2015 October 27 in a long-baseline configuration; S17 analyzed the one with CO. Both used J1550+0527 for flux and bandpass calibration. We adopted for it the flux model  $(S_{\nu}/\text{Jy}) = 1.000 \times (\nu/104.0 \text{ GHz})^{-0.602}$ , which is from the nearest records in the ALMA Calibrator Source Catalog, i.e., four measurements made at 91.5 and 233 GHz on October 31 and November 1.<sup>9</sup> We flagged three poorly performing antennas, DA45, DA65, and DV20, and used the remaining 37. The projected baseline lengths for Arp 220 ranged from 0.24 to 10.38 km for the first tuning with  $^{12}\text{CO}$  and from 0.22 to 11.10 km for the second with  $^{13}\text{CO}$ . We used CASA 4.7.2 for our data reduction (McMullin et al. 2007), starting from the raw data and following the steps of the observatory-provided calibration, except for the revised calibrator flux model and the

<sup>9</sup> The ALMA Observatory used the Morita Array (7 m array) for the quasar measurements, tied them to the measurements of Neptune, Mars, and Titan on the same days, and used the Butler–JPL–Horizons 2012 model for the solar system objects. The expected flux calibration accuracies in the ALMA Cycle 3 Proposer’s Guide are (better than) 5% and 10% for 92 GHz and 233 GHz, respectively. For our calibrator, the two measurements at each frequency agree quite well. As a result, the formal  $1\sigma$  uncertainties of our calibrator model are 0.004 Jy for the flux density and 0.10 for the spectral index after normalizing the power-law fit uncertainties so that the reduced  $\chi^2$  is unity. These uncertainties do not include any error due to deviation of the quasar spectral energy distribution from a power law and model uncertainties of the solar system objects. The Observatory used for the archived data products  $(S_{\nu}/\text{Jy}) = 1.126 \times (\nu/104.0 \text{ GHz})^{-0.680}$  for J1550+0527.

additional flagging of DA65 and DV20. We performed phase-only self-calibration using the continuum. It was first done independently for the two tunings, and we used that data for our visibility fitting. Another round was performed after combining the two data sets and before making the images presented in this paper.

## 3. 3 mm Spectra of the Two Nuclei

Figure 1 shows the spectra sampled at individual nuclei with  $0''.2$  and  $0''.1$  beams. The major lines in the spectra are  $^{12}\text{CO}(1-0)$ ,  $\text{CN}(1-0)$  doublet,  $\text{CH}_3\text{CN}(6-5)$ ,  $\text{HC}_3\text{N}(12-11)$ ,  $\text{HC}_3\text{N}(11-10)$ ,  $\text{CS}(2-1)$ , and  $\text{C}^{34}\text{S}(2-1)$ . The  $\text{HC}_3\text{N}$  lines include transitions within the vibrationally excited states  $v_7 = 1$  ( $l = 1e$  and  $1f$ ) and  $v_7 = 2$ .  $^{13}\text{CO}(1-0)$  and  $\text{C}^{18}\text{O}(1-0)$  are also in the frequency coverage but they are blended with other lines and are inconspicuous. Other likely identifications are  $\text{CH}_3\text{CCH}$  and  $\text{HC}_5\text{N}$ , while  $\text{H40}\alpha$  is not detected. These lines and more have been detected in emission in single-dish observations by Aladro et al. (2015). In the ALMA high-resolution data here, the  $\text{CN}$  doublet is almost totally in absorption while  $\text{CH}_3\text{CN}(6-5)$ ,  $\text{CS}(2-1)$ ,  $\text{C}^{34}\text{S}(2-1)$ , and  $\text{SO}(3_2-2_1)$  start to show absorption toward Arp 220 W at  $0''.1$  resolution. Although we will measure continuum source sizes later, this observation already indicates that the western nucleus has a bright continuum source or sources whose extent  $d$  satisfies  $d \lesssim 0''.1$  and  $d \ll 0''.1$ , because lines would have been in absorption at both resolutions if  $d \gtrsim 0''.2$  and in emission if  $d \ll 0''.1$ .

The continuum was first estimated by visually finding regions with the least lines in each spectrum and fitting a power-law curve  $S_{\nu} \propto \nu^{\alpha}$ ; off-line channels around 96–98, 107, and 109.5 GHz constrained the fit most. The obtained curves are plotted in Figure 1 and have power-law (i.e., spectral) indices  $\alpha \equiv d \log S_{\nu} / d \log \nu$  of  $+1.2$  for the western nucleus and  $0.0$  for the eastern nucleus with uncertainties of

about  $\pm 0.2$ . It is evident that the two nuclei have different spectral indices around 100 GHz. Arp 220 W has a positive index, indicating significant contribution from thermal dust emission or partially opaque free–free emission. Arp 220 E has a nearly flat spectrum, indicating much less contribution from such emission. Guided by these continuum fits and the observed spectra, we defined two sets of continuum-dominated channels (CDCs) for further analysis. The first (CDC<sub>1</sub>) is marked with black horizontal bars in Figure 1. They are more than  $650 \text{ km s}^{-1}$  from the systemic velocity for major lines but include weak possible lines such as HC<sub>5</sub>N. The total bandwidth of CDC<sub>1</sub> is 9.5 GHz. The contribution of line emission to the integrated emission of CDC<sub>1</sub> is in the range of 5%–10% for the two apertures and two nuclei. The second set of channels (CDC<sub>2</sub>) is marked with green bars in Figure 1. It is a subset of CDC<sub>1</sub> and avoids some weak lines.

#### 4. Visibility Fitting

We performed model fitting of the calibrated visibilities to obtain the continuum parameters of the two nuclei. Visibility fitting is a powerful way to analyze interferometric data when the target structure is simple and marginally resolved (e.g., Wiedner et al. 2002; Sakamoto et al. 2013).<sup>10</sup> For such cases, it is far more straightforward to fit visibilities than to make a dirty image first, deconvolve it next by iteratively finding clean components and convolving them with a clean beam, and then making an image-domain deconvolution of the cleaned image. We performed our nonlinear visibility fitting in IDL using an implementation of the Levenberg–Marquardt algorithm called mpfit (Moré 1978; Moré & Wright 1993; Markwardt 2009).

##### 4.1. 1G Fit

We first fitted the visibilities using one Gaussian component for each nucleus; we call this the 1G fit. The whole data set was fitted in each and every 30 MHz channel. The resulting parameters, averaged in CDC<sub>2</sub> to minimize line contamination, are listed in Table 1. Our 1G-fit positions agree very well with those measured at 33 GHz by BM15. Our 1G-fit parameters are consistent with the deconvolved parameters of S17 for Arp 220 E but we obtained a smaller size ( $0''.084 \times 0''.065$ ) and higher peak brightness temperature (386 K) for the more compact Arp 220 W, for which S17 obtained  $0''.12 \times 0''.11$  for the deconvolved FWHM and 167 K for the peak deconvolved  $T_b$ . Our visibility-fit size agrees with our image-domain deconvolved size from a  $0''.07$  resolution image made with `robust=0.5`.

##### 4.2. r2G fit

We next fitted each nucleus with the restricted two-Gaussian model (r2G fit) to see if we need more than one component for each nucleus. Minimally generalizing the 1G model, the r2G model has for each nucleus two elliptical Gaussians sharing the

<sup>10</sup> For example, a Gaussian source with 50 mas FWHM on the sky has a Gaussian-shaped distribution of the visibility amplitude centered at the origin of the  $uv$  plane, with the amplitude declining to 50% and 6% of the central value (=total flux) at  $uv$  radii of 0.9 and 1.8  $M\lambda$ , respectively. Our data coverage to about 3  $M\lambda$  is sufficient to determine the amplitude distribution in the  $uv$  domain and hence the source size in the image domain, provided that the visibilities have sufficient signal-to-noise ratio. Although our data set has a beam size of about 50 mas with the uniform weighting of visibilities, even smaller sizes can be measured from a precise amplitude-to- $uv$  radius curve (Martí-Vidal et al. 2012).

same center, axial ratio, and position angle. The shared parameters are fixed to the ones from the 1G fit. This model naturally defines an elliptic coordinate for each nucleus to plot visibilities as a function of the elliptic radius in the same manner as often done for a single axisymmetric source. For each nucleus, we first subtract the other nucleus and shift the phase center to the target nucleus, then we vector-average the visibilities in elliptical annuli and fit the real part of the visibilities. (In all other fitting in this section, complex visibilities were simultaneously fitted for the two nuclei without such subtraction.) The subtraction helps visualize the fit because otherwise the two nuclei create stripes in the visibility amplitude and phase in the  $uv$  plane. Without radial symmetry, any radial visibility plot will be less informative and harder to compare with models. We made two iterations to allow better nucleus subtraction. The subtracted models were first from the 1G fit and then from the r2G fit obtained in the previous iteration. Any subtraction residual causes visibility ripples with  $0.2 M\lambda$  spacing, which corresponds to  $1''$ . They tend to cancel out when averaged in an elliptical annulus larger than  $0.2 M\lambda$ . Since the cancellation is incomplete in smaller annuli, baselines shorter than  $0.2 M\lambda$  were flagged to suppress any subtraction residuals. The fitting was made for each of the nine sections of CDC<sub>2</sub>. All resulted in fits similar to an example in Figure 2, visually confirming that a single Gaussian is a poor fit for each nucleus while two (restricted) Gaussians can fit the data much better.

This result agrees with our observation at  $\sim 250$  and 350 GHz (K. Sakamoto et al. 2017, in preparation). It is also in line with the finding of BM15 that the 33 GHz (9 mm) continuum emission of the individual nuclei is better fitted (in the image domain) by an exponential disk than by a Gaussian, because an r2G model and an exponential disk share a central cusp and slow outer decline. On the other hand, at 3 mm, neither nucleus is fitted as nicely by a single elliptical exponential disk<sup>11</sup> as it is by the r2G model, although the difference is relatively small for Arp 220 E (see Figure 2).

##### 4.3. 2G Fit

After verifying that a single Gaussian provides a poor fit for each nucleus while two Gaussians perform much better, we fitted the continuum-dominated visibilities simultaneously using four Gaussians, two for each nucleus, without parameter restrictions (2G fit). Each Gaussian has six free parameters, one for the total flux density, two for position, and three for shape. The fits easily converged with reduced  $\chi^2$  of 1.4–2.1. Figure 3 shows that the fitted parameters agree well among the nine CDC<sub>2</sub> segments even though they are from two observing sessions with independent calibrations except for the common flux calibrator model. This ensures that our spatial decomposition is robust and not limited to the r2G model. Table 1 lists the averages of the derived parameters of the individual components. Denoting the smaller component in each nucleus with the subscript 1 and the larger with 2,  $E_1$  and  $W_1$  have major axis FWHMs of 88 mas

<sup>11</sup> An axisymmetric exponential disk with scale length  $a$ ,

$$f(x, y) = e^{-\sqrt{x^2+y^2}/a},$$

has the Fourier transform

$$\int_{-\infty}^{\infty} \int_{-\infty}^{\infty} f(x, y) e^{-i2\pi(ux+vy)} dx dy = \frac{2\pi a^2}{[1 + 4\pi^2 a^2 (u^2 + v^2)]^{3/2}}.$$

**Table 1**  
Arp 220 Parameters from the 3 mm Continuum

Parameter	Arp 220 E		Arp 220 W		Unit
One-Gaussian fit					
major axis FWHM	227 ± 5	...	83.5 ± 1.2	...	mas
minor axis FWHM	111 ± 1	...	64.6 ± 1.1	...	mas
axial ratio (min./maj.)	0.453 ± 0.007	...	0.765 ± 0.010	...	
major axis P.A.	47.4 ± 1.0	...	110.4 ± 1.1	...	°
peak $T_b$	37.3 ± 1.4	...	385.5 ± 7.4	...	K
R.A.(ICRS) <sup>a</sup> 15 <sup>h</sup> 34 <sup>m</sup>	57.2917	...	57.2224	...	s
Decl.(ICRS) <sup>a</sup> +23°30'	11.337	...	11.500	...	"
Two-Gaussian fit					
component name	$E_1$	$E_2$	$W_1$	$W_2$	
major axis FWHM	87.9 ± 3.6	369 ± 9	50.0 ± 0.7	232 ± 3	mas
minor axis FWHM	43.5 ± 3.5	188 ± 5	36.0 ± 0.5	144 ± 2	mas
axial ratio (min./maj.)	0.471 ± 0.033	0.505 ± 0.011	0.717 ± 0.010	0.617 ± 0.012	
major axis P.A.	55.0 ± 2.4	49.8 ± 1.1	136.1 ± 1.9	83.3 ± 0.4	°
peak $T_b$	72.8 ± 4.6	14.7 ± 0.7	639.9 ± 13.7	45.0 ± 1.5	K
R.A. offset <sup>b</sup>	-9.6 ± 0.8	12.0 ± 1.1	1.3 ± 0.1	-11.1 ± 0.7	mas
Decl. offset <sup>b</sup>	-1.4 ± 1.2	-1.2 ± 1.5	-1.2 ± 0.2	1.6 ± 0.6	mas
spectral index $\alpha^c$	-0.96 ± 0.92	0.81 ± 0.29	1.94 ± 0.16	1.01 ± 0.25	
1Gaussian + 1Exp-disk fit <sup>d</sup>					
component name	$E_1'$	$E_2'$	$W_1'$	$W_2'$	
major axis size <sup>e</sup>	$\lesssim 70$	82.1	55.7 ± 1.3	56.9	mas
minor axis size <sup>e</sup>	$\lesssim 50$	43.6	32.9 ± 1.6	33.9	mas
axial ratio (min./maj.)	...	0.531	0.583 ± 0.020	0.596	
major axis P.A.	...	54.7	144.8 ± 1.9	79.4	°
peak $T_b$	...	...	529 ± 20	...	K
R.A. offset <sup>b</sup>	...	0	0.67 ± 0.16	0	mas
Decl. offset <sup>b</sup>	...	0	-0.97 ± 0.09	0	mas
spectral index $\alpha$	...	-0.59	3.57 ± 0.21 <sup>f</sup>	-0.61	

**Notes.** Parameters were obtained with visibility fitting. Fitting results from the nine segments of the continuum-dominated channels (CDC<sub>2</sub>) were averaged using the inverse square of their uncertainties as weights. The uncertainties of the means here are  $\pm 1\sigma$  and do not include any systematic errors. The peak (Rayleigh–Jeans) brightness temperatures are subject to the flux calibration uncertainty on the order of 5% in this ALMA band.

<sup>a</sup> Absolute astrometry is estimated to be accurate to 5 mas from the visibility-fit positions of the test source J1532 + 2344 in the same observations.

<sup>b</sup> Offset from the one-Gaussian fit position.

<sup>c</sup> Unaccounted errors due to low-level line contamination are expected for components with low brightness temperatures.

<sup>d</sup> Parameters for the exponential disks  $E_2'$  and  $W_2'$ , in italics, are from BM15 and fixed.

<sup>e</sup> Gaussian FWHM for  $E_1'$  and  $W_1'$  and exponential scale length for  $E_2'$  and  $W_2'$ . For comparison between a Gaussian and an exponential disk, the half-light diameter of a Gaussian is its FWHM and that of an exponential disk is about 3.36 times the exponential scale length.

<sup>f</sup> This spectral index is a consequence of an assumption about the spectral index of dust emission (Section 6.2). See Section 6.3 for a caution about this assumption.

(36 pc) and 50 mas (21 pc), respectively. Their peak brightness temperatures are as high as 73 K in  $E_1$  and 640 K in  $W_1$ . They are more than twice smaller in size and warmer in brightness temperature than the single-Gaussian estimates in S17. The larger components  $E_2$  and  $W_2$  have major axis FWHMs  $0''.37$  and  $0''.23$  (about 150 and 100 pc) and peak brightness temperatures of 15 and 45 K, respectively.  $W_1$  and  $W_2$  have their major axes misaligned by about  $50^\circ$  while the eastern nucleus is reasonably fit with two Gaussians sharing virtually the same axial ratio and position angle. In each nucleus, the compact and extended components are almost concentric, with only 13–22 mas (5–9 pc) offsets between their centroids. It is noteworthy that the spectral index of  $W_1$ ,  $1.94 \pm 0.16$ , is consistent with that of the Rayleigh–Jeans part of optically thick emission, although the index can instead be due to a superposition of multiple kinds of emission with different spectral indices. The compact components  $E_1$  and  $W_1$  have about 20% and 47% of the 3 mm flux densities of the individual nuclei, respectively. Finally, we verified our 2G fitting by using data before any self-calibration. The sizes changed little and within

the listed  $1\sigma$  uncertainties. The largest change in peak  $T_b$  was only a 5% reduction for  $W_1$  to  $607 \pm 14$  K.

#### 4.4. 1G+1E Fit

We performed further fitting for parameters of the dust emission in the nuclei. Plasma emission, i.e., synchrotron and free–free emission, dominates at 33 GHz and was fitted well in each nucleus as an exponential disk (BM15). We therefore employed two exponential disks having the parameters of the plasma disks (see Table 1), fractional contributions of the plasma and dust emission at 3 mm as we estimate in Section 6.2, and two Gaussians without fixed parameters. Each nucleus is therefore described as an exponential disk of fixed parameters plus a Gaussian (1G+1E fit). We refer to the Gaussian dust components in the two nuclei as  $E_1'$  and  $W_1'$  and to the plasma disks as  $E_2'$  and  $W_2'$ . The employed flux contributions of the dust emission are  $E_1'/E = 13\%$  and  $W_1'/W = 41\%$  at 3 mm. This 1G+1E fitting only provided an upper limit on the size for the dust component in Arp 220 E but the limit is comparable to the size of  $E_1$  in the 2G fit. Because

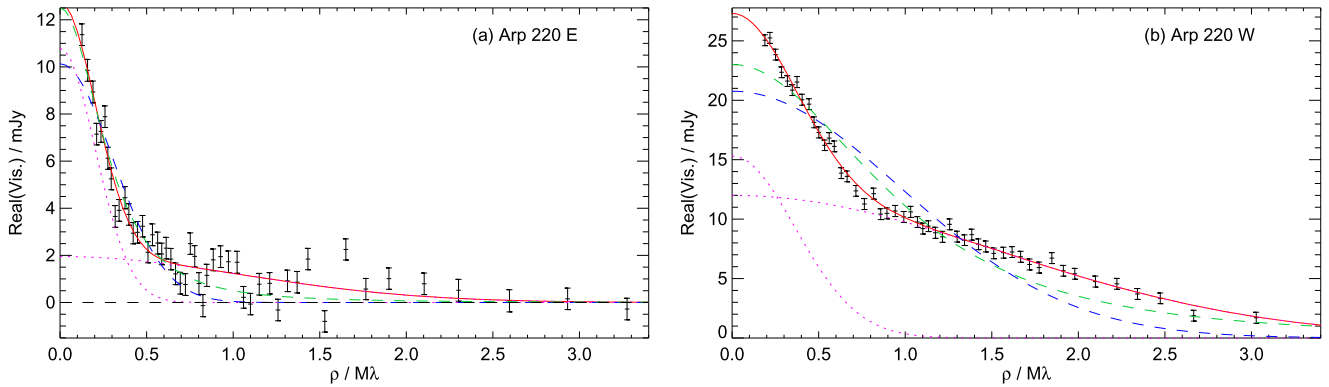


**Figure 2.** Arp 220 visibility fitting results for continuum-dominated channels around 112.6 GHz (a segment of CDC<sub>2</sub>). The real part of the visibilities is plotted as a function of the semiminor axis of the elliptic coordinate in the  $uv$  plane (see the text for the fitting procedure). The data error bars are  $\pm 1\sigma$ . The magenta dotted curves are the two Gaussians whose sum, the red curve, best fits the data. The fitted major axis FWHMs ( $\theta_{\text{maj}}$ ) at this frequency are the following. East nucleus:  $\theta_{\text{maj}}^{(1)} = 74 \pm 16$  mas and  $\theta_{\text{maj}}^{(2)} = 381 \pm 27$  mas. West nucleus:  $\theta_{\text{maj}}^{(1)} = 50 \pm 1$  mas and  $\theta_{\text{maj}}^{(2)} = 212 \pm 7$  mas. For comparison, the blue and green dashed curves show the best fits with a single Gaussian and an exponential disk, respectively.

$E_1$  has  $\sim 20\%$  of the 3 mm flux density in the eastern nucleus while  $E_1'$  has 13%, we see that  $E_1 \sim E_1'$ . We obtained consistent results for Arp 220 W over the CDC<sub>2</sub> segments, and the averaged parameters are in Table 1. The dust component  $W_1'$  has a spectral index of  $3.57 \pm 0.21$  as a direct consequence of our assumed spectral index of  $\alpha_d = 3.8$  for the dust emission. Except for the spectral index, the parameters of  $W_1'$  are close to those of the component  $W_1$  in our 2G fit including the flux density fraction of  $W_1/W = 47\%$ , hence  $W_1 \approx W_1'$ . Combining the results for the two nuclei, the compact components in our 2G fit represent mostly dust emission peaking at the centers of the two nuclei while the larger components in the individual nuclei correspond to the exponential (circum)nuclear disks with dominant plasma emission. We are going to further discuss the decomposition in Section 6.

## 5. Images

We made continuum images from the continuum-dominated channels CDC<sub>1</sub> introduced in Section 3. Multifrequency synthesis was performed with two terms (i.e., the spectrum at each position is assumed to follow a power law) and using the robust weighting (Briggs 1995).

Figure 4 shows the 3 mm continuum images made with three different robust parameters. The dominant features in all images are a bright compact source at the center of Arp 220 W ( $W_1$  in our 2G fit) and larger elongated structures in the position angles of about  $50^\circ$  in E and  $80^\circ$  in W ( $E_2$  and  $W_2$ , respectively). Arp 220 E also has a compact central component ( $E_1$ ) that is easier to see in panel (c) with the highest resolution and equal-step contours at lower levels. The overall structure is consistent with our visibility fitting results. The peak intensities in the maps are lower than our fitted values as expected from beam dilution.

Looking for features that could not be captured by our simple models, we find in Figure 4(a) that the western nucleus has faint bipolar features that extend from the central region along P.A.  $\sim 170^\circ$  and perpendicular to the major axis of  $W_2$ . This feature is below the lowest contour in the continuum image of S17, which corresponds to our third contour. The eastern nucleus also shows faint features in panel (a) around the tips of its major axis, extending in opposite directions like an integral sign. This is also seen at 33 GHz (BM15). In

panels (b) and (c), we see that the extended component  $E_2$  starts to be resolved into multiple sources. This may also be the case for  $W_2$  in the panel (c).

Figure 4(b') compares the 3 mm continuum emission with the distribution of compact ( $< 2$  pc) radio (18–2 cm) sources that were observed over 1994–2014 with VLBI (Varenius et al. 2017 and references therein). These sources have almost been entirely attributed to supernovae, i.e., radio supernovae and young supernova remnants (Smith et al. 1998; Lonsdale et al. 2006; Parra et al. 2007; Batejat et al. 2011; Varenius et al. 2017). The VLBI source distribution is similar to the 3 mm emission distribution in both nuclei, mainly following the larger  $E_2$  and  $W_2$  components. The similarity was also seen by BM15 in 33 GHz plasma emission at a comparable resolution of  $0''.07$ .

## 6. Further Analysis and Discussion

### 6.1. Nuclear Disks and Outflow from Arp 220 W

We ascribe the larger components ( $E_2$  and  $W_2$ ) in our two-Gaussian (2G) model to the nuclear disks of Arp 220 that rotate around the individual nuclei (Sakamoto et al. 1999). We attribute the elongation of these components on the sky to the disk inclinations and suggest that the faint feature perpendicular to the major axis of the western nuclear disk is a bipolar outflow.

The (counter-)rotating nuclear disks have been seen through velocity gradients along their major axes in high-resolution line imaging (Sakamoto et al. 1999, 2008; Scoville et al. 2015, 2017). If the disks are thin, then their inclinations can be calculated from their axial ratios to be  $60^\circ$  for  $E_2$  and  $52^\circ$  for  $W_2$ , which agree with the estimates of BM15 for  $E_2'$  and  $W_2'$ . At least our inclination for the western nuclear disk is a lower limit because the outflow emission biases the measured axial ratio, and the outflow-driving activity in the disk should give it a thickness. We thus estimate  $i \approx 60^\circ$  for both disks. An apparent minor-to-major axis ratio of 0.62 for the western nuclear disk translates to an inclination in the range of  $60^\circ \pm 10^\circ$  for an oblate spheroid having a height-to-radius ratio up to 0.55. On the western nuclear disk, we therefore differ with S17, who, without seeing the faint bipolar component, modeled it as a thin face-on disk with  $i \approx 30^\circ$ . The CO velocity field in their Figure 4 does suggest a nearly face-on configuration if the gas distribution is two dimensional. However, a similar velocity field can be due to a three-dimensional bipolar outflow

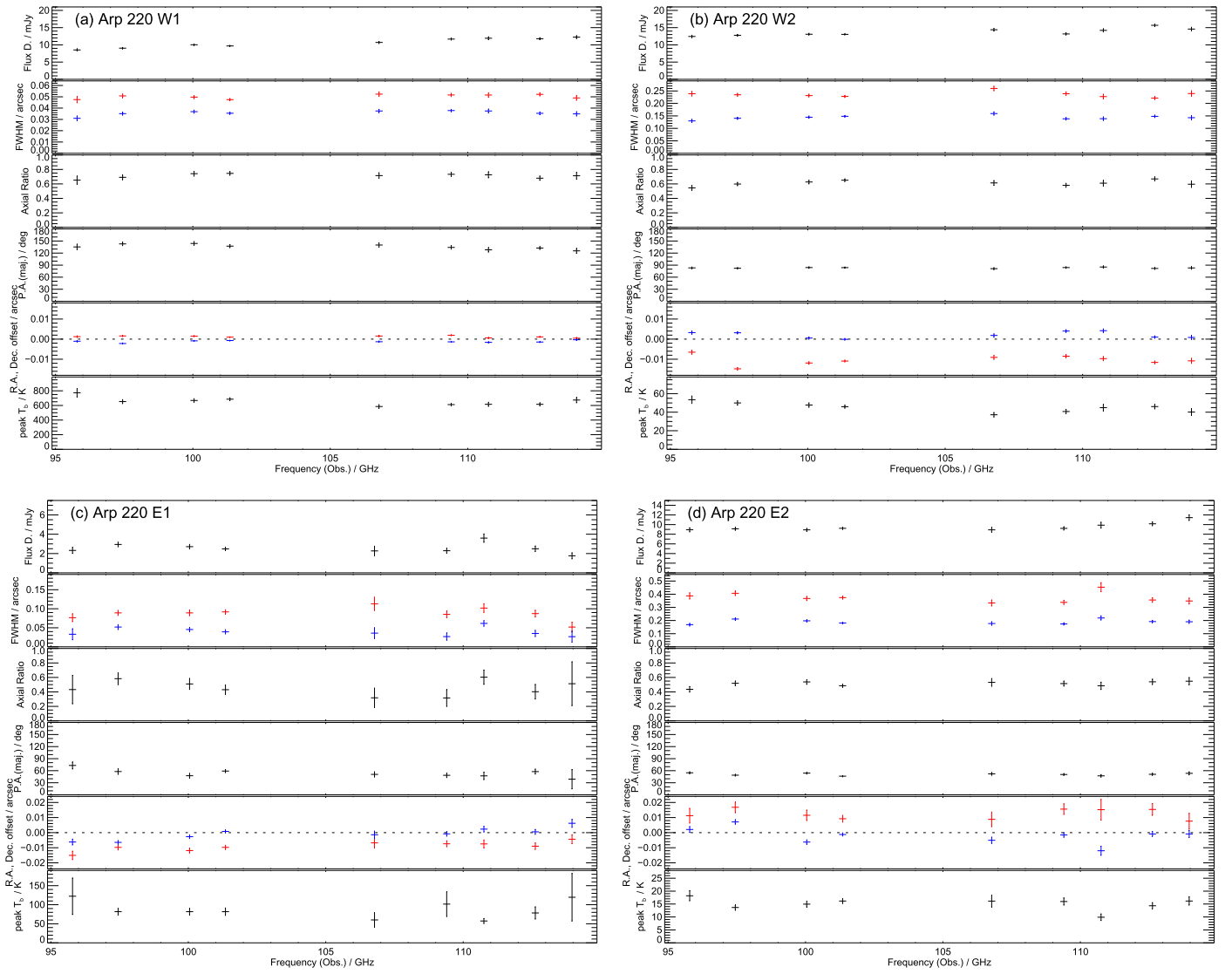


**Figure 3.** Arp 220 visibility fitting results for selected continuum-dominated channels ( $CDC_2$ ). Visibilities were fitted with four elliptical Gaussians, two for each nucleus (2G fit). The six parameters of each Gaussian and two derived from them (axial ratio and peak brightness) are plotted. Panels (a) and (b) show the smaller and larger of the two Gaussians, respectively, fitting the west nucleus. Panels (c) and (d) are for the east nucleus. The six subpanels for each Gaussian show, from top to bottom, the source-integrated flux density, major (red) and minor (blue) axis FWHMs, minor-to-major axial ratio, position angle of the major axis, positional offset (red for R.A. and blue for decl.) from the 1G-fitting position of the nucleus, and the peak Rayleigh–Jeans brightness temperature of the component. Error bars are  $\pm 1\sigma$  rescaled so that the reduced  $\chi^2$  will be unity at each frequency. The data used to create this figure are available.

seen from the side (Seaquist & Clark 2001; Walter et al. 2002). Therefore, while it remains to be seen whether the CO data cube can be reasonably fitted with a three-dimensional outflow model, at least one projection of the cube (i.e., the mean velocity map) is consistent with a nearly edge-on outflow. The large inclination of the western nuclear disk explains the alignment of the supernova features (Figure 4(b’)), which posed difficulty in S17’s face-on disk model because any alignment at the time of star formation would be erased in the differentially rotating disk by the time of supernova explosions. The large inclination of the western nuclear disk had been the preferred model until S17; Scoville et al. (1998) inferred it from near-infrared imaging with the *Hubble Space Telescope*.

Molecular outflow from the individual nuclei of Arp 220, in particular from W, has been known from P-Cygni line profiles and blueshifted line absorption (Sakamoto et al. 2009; Rangwala et al. 2011; González-Alfonso et al. 2012;

Veilleux et al. 2013; Tunnard et al. 2015; Martín et al. 2016; Barcos-Muñoz 2016; Zschaechner et al. 2016), which is also evident in the high-resolution spectrum in Figure 1 for the western nucleus. Sakamoto et al. (2009) also noted that the OH masers observed by Rovilos et al. (2003) show a bipolar distribution around the western nucleus along its disk minor axis in the north–south direction, as one would expect for an outflow from the nuclear disk. Tunnard et al. (2015) proposed this to be the actual outflow configuration on the basis of their finding that SiO(6–5) at the systemic velocity is in absorption to the south and in emission to the north of the nucleus. Varenus et al. (2016) further detected a north–south extension of the 150 MHz emission around the western nucleus at  $\sim 0''.5$  resolution and attributed it to a bipolar outflow of the same configuration. Barcos-Muñoz (2016) found that a spectral index map between 33 and 92 GHz at  $\sim 0''.08$  resolution has a distinct positive-value region across the western nuclear disk

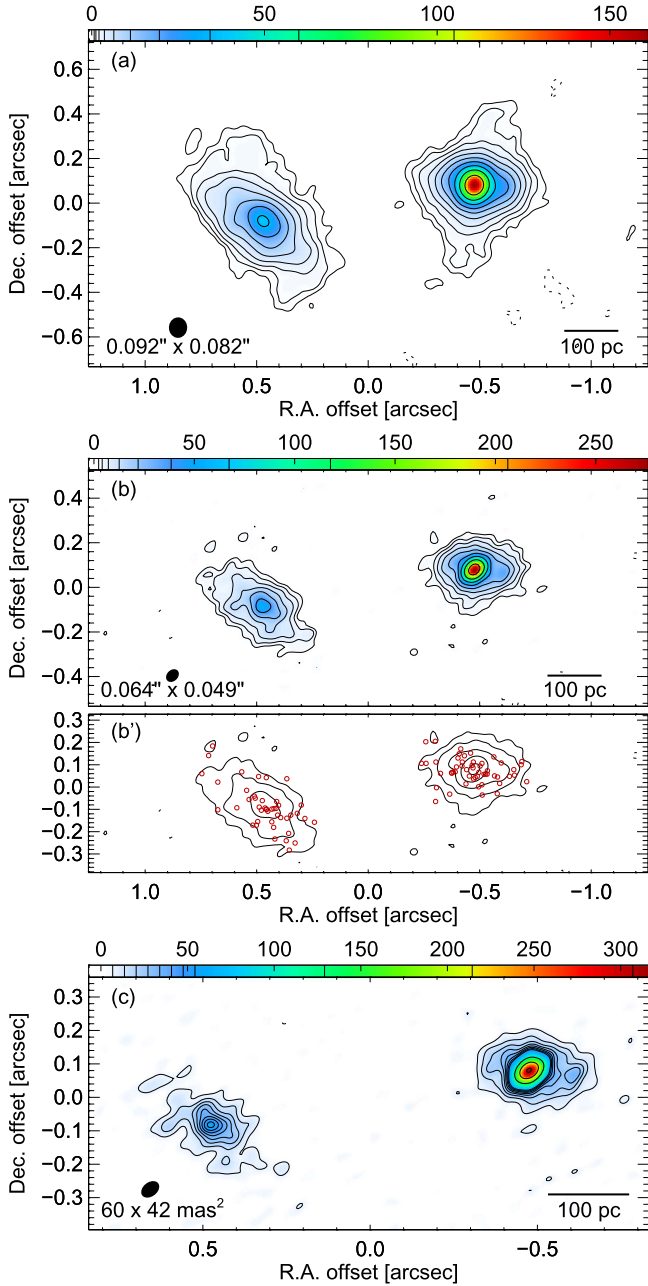


**Figure 4.** Arp 220 continuum images at 104.1 GHz (2.9 mm). Each panel shows the FWHM beam size on the bottom-left corner. The offset coordinates are from the midpoint of the two nuclei. The intensity unit of the color bars is Kelvin (Rayleigh–Jeans brightness temperature). (a) Imaged with `robust=2`, i.e., the natural weighting. The  $n$ th contour is at  $\pm 3n^{1.75}\sigma$ , where  $\sigma = 0.23$  K ( $15 \mu\text{Jy beam}^{-1}$ ). The peak intensity is 161 K ( $10.8 \text{ mJy beam}^{-1}$ ). Negative contours are dashed. (b) Imaged with `robust=0`. The  $n$ th contour is at  $\pm 3n^{1.75}\sigma$ , where  $\sigma = 0.78$  K. The peak intensity is 276 K. (b') The same image as (b) but with every other contours. Overplotted are compact ( $< 2$  pc) radio VLBI continuum sources (Varenius et al. 2017). (c) Imaged with `robust=-1`. The  $n$ th contours are at  $\pm 3n\sigma$  ( $1 \leq n \leq 8$ ) and  $3 \times 8(n-7)^{1.25}\sigma$  ( $8 \leq n$ ), where  $\sigma = 2.3$  K. The peak intensity is 57 K in Arp 220 E and 316 K in Arp 220 W.

along P.A.  $\sim 153^\circ$ . Our observation of a bipolar structure in the 3 mm continuum is consistent with these observations and corroborates the outflow from Arp 220 along P.A.  $\sim 170^\circ$ . Further evidence supporting this outflow will be presented in L. Barcos-Muñoz et al. (2017, in preparation).

In light of the revived picture of a highly inclined disk plus a bipolar outflow for the western nucleus, we notice that the CO

maps of the nucleus in S17 (their Figure 4) show a bipolar feature corresponding to that in the 3 mm continuum. Its southern part is more prominent and blueshifted. Tunnard et al. (2015) already proposed that the southern side of the bipolar outflow is approaching us, i.e., blueshifted. For this velocity structure, the southern side of the western nuclear disk must be its far side if the outflow axis is normal to the disk. This is at odds with the near-infrared observation that the southern side has a much larger extinction and should be the near side of the nuclear disk (Scoville et al. 1998). Therefore, unsolved problems about the detailed configuration of the outflow and the inner structure of the western nuclear disk remain. It may be that the outflow axis is not perpendicular to the disk but only in the plane containing the disk rotation axis and our sight line, or the disk may be warped. Regarding the outflow driver, both nuclear disks at least have vigorous star formation as traced by the VLBI supernovae. In addition, the core component  $W_1$ , with its very high luminosity surface density (see Section 6.5), probably makes a large or even dominant contribution to drive the outflow. The outflow has oblique angles with respect to the major and minor axes of  $W_1$  (and  $W_1'$ ), while it is orthogonal to the  $W_2$  major axis. This implies a role of the nuclear disk in the outflow collimation, but, as noted above, a three-dimensional configuration of the system is necessary to verify this. On Arp 220 E, although blueshifted absorption was also detected toward it, the lack of a bipolar feature at 3 mm in this nucleus despite both nuclear disks apparently having large inclinations suggests that the outflow from the eastern nucleus has less mass or less 3 mm emissivity or both.

## 6.2. Fractional Contribution of Dust Emission

We estimate from spectral indices that the fractional contribution of dust emission to the 3 mm continuum is  $f_d \approx 13\%$  and  $41\%$  for Arp 220 E and W, respectively. If dust emission with a spectral index  $\alpha_d$  makes a fractional contribution  $f_d$  to the observed flux density, and the rest of the emission from plasma, which is the sum of synchrotron and free-free emission, has a spectral index  $\alpha_p$ , then the total emission has a spectral index of  $\alpha = f_d \alpha_d + (1 - f_d) \alpha_p$ .<sup>12</sup> We use  $\alpha_d = 3.8$  for optically thin dust emission using the dust emissivity index  $\beta$  of  $1.8 \pm 0.1$  in the Galactic plane (Planck Collaboration et al. 2011), and  $\alpha_p = -0.59 \pm 0.08$  for E and  $-0.61 \pm 0.07$  for W from the 6–33 GHz measurements by BM15. With the overall 3 mm spectral indices that we estimated from Figure 1, we obtain  $f_d = 0.13 \pm 0.04$  and  $0.41 \pm 0.05$  for Arp 220 E and W, respectively. The errors do not include the effect of any variation of the plasma spectral index between 6 and 33 GHz and  $\sim 100$  GHz. Although  $\alpha_p$  likely increases at higher frequencies as the fractional contribution of the free-free emission increases, its effect on  $f_d$  should be small because BM15 found from centimeter wave data that synchrotron emission dominates at 33 GHz (and

<sup>12</sup> A spectrum that consists of power-law spectra having spectral indices  $\alpha_i$  and fractional contributions  $w_i$  at a reference frequency  $\nu_0$ ,

$$S_\nu = S_{\nu_0} \sum_i w_i \left( \frac{\nu}{\nu_0} \right)^{\alpha_i}, \quad \text{where } \sum_i w_i = 1,$$

has the spectral index

$$\alpha = \frac{d \log S_\nu}{d \log \nu} \Big|_{\nu=\nu_0} = \left[ \frac{\nu}{S_\nu} \frac{d S_\nu}{d \nu} \right]_{\nu=\nu_0} = \sum_i w_i \alpha_i$$

at the reference frequency.

attributed the weakness of the free–free emission to the dust absorption of ionizing photons). For example, if synchrotron emission has a constant spectral index  $-0.7$  and free–free emission at  $-0.1$ , then the fractional contribution of synchrotron to the 33 GHz continuum having  $\alpha = -0.6$  should be  $5/6 = 83\%$ . The synchrotron fraction decreases only slightly to 71% and  $\alpha_p$  increases only slightly to  $-0.53$  at 104 GHz. For this  $\alpha_p$ , the dust contribution to the 3 mm continuum will decrease only by 0.01 for each nucleus. Likewise, if part of the dust emission is saturated (i.e., opacity  $\gtrsim 1$ ) at 3 mm or the dust  $\beta$  is smaller than assumed (e.g., the median  $\beta$  is 1.6 in single-temperature fits for a sample of ULIRGs; Clements et al. 2010), then  $f_d$  increases slightly by only 0.01 for E and 0.03 for W for  $\alpha_d = 3.5$ . It is notable that for each nucleus the estimated fraction of dust emission broadly agrees with the flux density fraction of the compact component in our 2G fit, 20% for E and 47% for W (Section 4.3).

One could also estimate dust emission by subtracting the plasma component from the observed total emission. Arp 220 E and W should have 104.1 GHz flux densities of  $15.1 \pm 2.3$  and  $16.4 \pm 2.4$  mJy, respectively, from synchrotron and free–free emission if we extrapolate the 33 GHz flux densities with the 6–33 GHz spectral indices in BM15. The errors include a 12% absolute flux calibration uncertainty at 33 GHz. The ALMA total flux densities at the same frequency are estimated to be  $11.9 \pm 0.9$  and  $23.9 \pm 1.3$  mJy, for E and W, respectively, from the 2G fit assuming a power law among the nine frequency segments; the uncertainties include a 5% error in absolute flux scale. Nominally,  $f_d$  is calculated from these flux densities to be  $-0.27$  and  $0.31$  in Arp 220 E and W, respectively. The unphysical negative fraction may be simply because the denominator or numerator or both are in error; the fraction could be zero if both are in error by  $1\sigma$  from the estimates above. Other possible sources for error include the flux calibration both at VLA and ALMA, missing flux in ALMA data that may be larger for a more extended eastern nucleus, and change in the spectral index of the plasma emission between 33 and 100 GHz. Because the previous method to estimate  $f_d$  from the spectral indices alone is not affected by the first two of these errors, we adopt the  $f_d$  estimates in the previous paragraph. We note that S17, despite using this direct subtraction method, could obtain  $f_d$  of 0.11 and 0.45, respectively for E and W at 112.6 GHz. Our adopted estimates agree with theirs.

### 6.3. Distribution of Dust Emission in the Nuclei

We can estimate the spatial distribution of the dust emission in the nuclei by subtracting the plasma emission. For the latter emission, we use the exponential disks that BM15 fitted to the Arp 220 nuclei at 33 GHz. We adopt their deconvolved shapes, place the plasma disks in our 1G-fit positions, and scale the model flux densities to be consistent with the ALMA flux densities of the nuclei multiplied by their adopted  $(1 - f_d)$ . Within the 100 GHz band, we assume that the plasma disks retain their 33 GHz spectral indices.

Figure 5 is a dust emission map made using all  $\text{CDC}_2$  data. The dust emission in each nucleus has the strongest peak at the center and also has weaker peaks around it. The central concentration of the dust emission is much more pronounced than that of the VLBI sources in both nuclei and in particular in the western nucleus. This compactness of dust emission compared to the VLBI supernova distribution in Arp 220 W

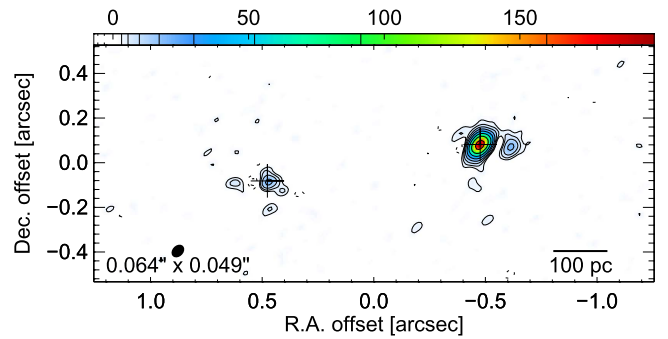


**Figure 5.** Arp 220 dust-continuum emission at 104.1 GHz (2.9 mm). It is estimated by subtracting the plasma emission in the form of elliptical exponential disks measured at 33 GHz. This image was made with `robust=0` after the subtraction in the  $uv$  domain. The FWHM beam size is at the bottom-left corner. The offset coordinates are from the midpoint of the two nuclei. The crosses are at the continuum 1G-fit positions in Table 1. The  $n$ th contour is at  $\pm 3n^{1.75}\sigma$ , where  $\sigma = 1.06$  K ( $30 \mu\text{Jy beam}^{-1}$ ). Negative contours are dashed. The peak intensity is 20 K in Arp 220 E and 199 K in Arp 220 W. The intensity unit of the color bar is Kelvin (Rayleigh–Jeans brightness temperature).

was already noted at 0.86 mm (Sakamoto et al. 2008). The central peak of the 3 mm dust emission is much stronger in Arp 220 W than in Arp 220 E. This partly corresponds to the larger fractional contribution of dust emission in Arp 220 W ( $\sim 41\%$  at 3 mm) than in Arp 220 E ( $\sim 13\%$ ). The weaker peaks around the central ones may be dust emission from the nuclear disks but some of them can be residual plasma emission because we only subtracted its parametrized approximation. We also caution about an underlying assumption in this subtraction that all emission is optically thin. If the dust emission toward the center of a nucleus is optically thick, then it is unnecessary to subtract plasma emission from behind the dust photosphere because such emission does not reach us in the first place. It is therefore possible that the dust emission peaks are more pronounced than seen in Figure 5 at the centers of the two nuclei, in particular the western nucleus where the spectral index of  $W_1$  is compatible with optically thick emission.

We already obtained the parameters of the dust emission through the visibility fitting with the 1G+1E model (Section 4.4). In the fitting, the parameters of the model exponential disks were fixed to those of the plasma emission. The results for the Gaussian (dust) components are consistent with our image-domain estimate for dust emission regarding the presence of compact peaks at the centers of the two nuclei. The caution about the possible oversubtraction toward the center of the western nucleus applies to this visibility fitting, too. The peak brightness temperature of the dust emission at the center of the western nucleus,  $\gtrsim 500$  K, is more than twice higher than any previous measurements of dust brightness temperature in Arp 220. For example, Downes & Eckart (2007,  $\sim 90$  K), Sakamoto et al. (2008,  $\sim 160$  K), Wilson et al. (2014,  $\sim 200$  K), and Scoville et al. (2017,  $\sim 120$  K) all reported deconvolved peak brightness temperatures of dust continuum only up to 200 K with a single-Gaussian deconvolved FWHM of  $\sim 0''.1$ – $0''.2$ . There have been, however, pieces of spectroscopic evidence for much warmer dust and molecular gas in the galaxy (e.g., Martín et al. 2011; Rangwala et al. 2011; González-Alfonso et al. 2012, 2013).

#### 6.4. Bolometric Luminosity of the Compact Core in the Western Nucleus

The bolometric luminosity of the compact core found in the western nucleus can be estimated as follows for its thermal dust emission. A geometrically thin and optically thick disk with a radial temperature described by a Gaussian falloff has a bolometric luminosity of

$$\begin{aligned} L_{\text{bol}} &= 2 \int_{-\infty}^{\infty} \int_{-\infty}^{\infty} \sigma \left[ T_p \exp \left( -\log 2 \frac{x^2 + y^2}{r_{\text{maj}}^2} \right) \right]^4 dx dy \\ &= \frac{\pi r_{\text{maj}}^2 \sigma T_p^4}{2 \log 2} \\ &= 3.2 \times 10^9 \left( \frac{r_{\text{maj}}}{10 \text{ pc}} \right)^2 \left( \frac{T_p}{100 \text{ K}} \right)^4 L_{\odot}, \end{aligned} \quad (1)$$

where the factor of 2 before the integral is for the two faces of the disk,  $\sigma$  is the Stefan-Boltzmann constant,  $T_p$  is the peak dust temperature, and  $r_{\text{maj}}$  is the (major axis FWHM)/2 of the Gaussian temperature distribution in linear scale. For  $W_1'$ , we obtain  $L_{\text{bol}} = (3.3 \pm 0.8) \times 10^{12} L_{\odot}$  from  $r_{\text{maj}} = 11.5 \pm 0.3$  pc and  $T_p = 529 \pm 20$  K as well as a 5% absolute flux-scale uncertainty. Here, the brightness temperature of the dust emission is equated with the dust physical temperature. This  $L_{\text{bol}}$  is four times larger than the one for the western nucleus by Wilson et al. (2014), who used the same formula and 0.43 mm data ( $T_p = 197$  K and  $r_{\text{maj}} = 41$  pc scaled to our adopted distance), and is 1.7 times larger than the  $L_{8-1000 \mu\text{m}}$  of Arp 220.

There are cautions for and limitations in the luminosity estimate and comparison above. First, our subtraction of plasma emission assumed that the dust (as well as plasma) emission is optically thin at 3 mm while the calculation above assumes an optically thick emitter. Even if the dust emission around the peak has a 3 mm opacity below unity, it cannot be much below this because dust cannot be hotter than its sublimation temperature; one obtains  $\tau_{3\text{mm}} > 0.25$  from  $\max(T_b)/\tau_{3\text{mm}} \approx T_{\text{dust}} < 2000$  K. The dust is therefore expected to become optically thick at shorter wavelengths not far from 3 mm because of the wavelength-dependent opacity coefficient. Observations at shorter wavelengths also suggest so (Sakamoto et al. 2008; Wilson et al. 2014). In such a situation, the bolometric luminosity of the  $W_1'$  component can be higher than the calculation above because at shorter wavelengths where most of the luminosity is radiated, the nucleus can radiate at a higher brightness temperature than at 3 mm, at  $T_{\text{dust}}$  instead of  $(1 - e^{-\tau})T_{\text{dust}}$ . To rectify this, we can adopt the assumption that the 3 mm continuum toward the center of Arp 220 W is optically thick, which is consistent with the spectral index of  $W_1$  in the 2G fit. Using the  $W_1$  parameters, the bolometric luminosity of the core is calculated to be  $(5.7 \pm 1.2) \times 10^{12} L_{\odot}$ . Second, the total luminosity from Equation (1) integrates direction-dependent radiation from the disk over the entire directions whereas the observational source luminosity  $L_{8-1000 \mu\text{m}}$  is based on our measurements from a single direction and is calculated assuming isotropy. The latter luminosity can be biased for a disk-like source with anisotropic radiation. Most of the bolometric luminosity of Arp 220 is observed at mid-to-far-infrared wavelengths around 50  $\mu\text{m}$ . Hence, most of the luminosity from the 500 K core is absorbed

and re-radiated before reaching us, presumably in large part by the nuclear disk  $W_2$ . Because we look at  $W_2$  (as well as  $E_2$ ) from the side, i.e., from directions with less flux, the  $L_{8-1000 \mu\text{m}}$  of Arp 220 may well be underestimated. Third, we assumed that each nucleus is an axisymmetric disk to derive its inclination and luminosity, but this may not be valid. Removing this assumption, the lowest disk luminosity can be obtained by replacing  $r_{\text{maj}}^2$  with  $r_{\text{maj}}r_{\text{min}}$  in Equation (1). It is  $(1.9 \pm 0.5) \times 10^{12} L_{\odot}$  for  $W_1'$ , which agrees with the  $L_{8-1000 \mu\text{m}}$  of Arp 220. This is the limiting case in which  $W_1'$  is an oval-shaped disk observed face on. Fourth, the true distribution of the brightness temperature in  $W_1$  as well as  $W_1'$  may not be Gaussian and may be more flat-topped. Or it may be that the 33 GHz emission has a weak central cusp in addition to the exponential disk but it was missed in the observations at 0".07 resolution. If it were due to opaque free-free emission, then it can become significant at 100 GHz. Because of the  $\propto T^4$  dependence,  $L_{\text{bol}}$  in these cases would be smaller than the calculations above.

To summarize, the bolometric luminosity of the dust thermal emission from the central component in Arp 220 W is estimated to be  $\sim 10^{12.5} L_{\odot}$  with at least  $\pm 0.2$  dex uncertainty due to various assumptions. It is as large as most of the bolometric luminosity of Arp 220 and may even exceed the  $L_{8-1000 \mu\text{m}}$  of Arp 220 estimated from our vantage point. Higher-resolution data will help improve the luminosity estimate by better constraining the shape and temperature of the core. More frequency coverage will also help to better extract dust thermal emission from the mixture of dust continuum, synchrotron, free-free, and line emission at millimeter and submillimeter wavelengths. In passing, we add that the dust temperatures in  $E_1'$  and the two nuclear disks are very likely higher than their low brightness temperatures in 3 mm dust emission because dust is probably optically thin in these components. If so, they may also have considerable luminosities that will be better constrained with observations at shorter wavelengths.

#### 6.5. Luminosity Source and Evolution of the Western Nucleus

The high peak intensity of the continuum emission at the center of Arp 220 W constrains the luminosity source, with the caveats in the preceding section. The peak brightness temperature of the dust thermal emission,  $T_p = 5.3 \times 10^2$  K for the  $W_1'$  component, translates to a peak luminosity surface density of  $\sigma T_p^4 = 1.1 \times 10^{16} L_{\odot} \text{ kpc}^{-2}$ . Since we do not know the fine details of the spatial distribution of the continuum emission, the means in the half-light diameter (=FWHM for a Gaussian) are more robust than the peak values, namely, the mean brightness temperature  $\langle T_b \rangle_{1/2} = 3.8 \times 10^2$  K and mean luminosity surface density  $\sigma(\langle T_b \rangle_{1/2})^4 = 3 \times 10^{15} L_{\odot} \text{ kpc}^{-2}$  in the central 23 pc. For comparison, Soifer et al. (2003) obtained from mid-IR observations of three Seyfert nuclei the surface brightnesses of  $(1 - 5) \times 10^{14} L_{\odot} \text{ kpc}^{-2}$  at similar linear scales (10–30 pc). The surface brightnesses of infrared-luminous starburst galaxies and Galactic H II regions are typically an order of magnitude (or more) below these Seyfert values (Soifer et al. 2001; Evans et al. 2003). Barcos-Muñoz et al. (2017) estimated luminosity surface densities in the 33 GHz half-light radii (30 pc to 1.7 kpc) for 22 local ultra/luminous infrared galaxies including those with AGNs. Their maximum value is  $1 \times 10^{14} L_{\odot} \text{ kpc}^{-2}$  and the mode is at  $1 \times 10^{13} L_{\odot} \text{ kpc}^{-2}$ . This agrees with earlier analysis by Thompson et al. (2005), who not

only showed statistics on IR-luminous galaxies but derived  $10^{13} L_{\odot} \text{ kpc}^{-2}$  as a characteristic value for warm starbursts ( $T < 200$  K) constrained by radiation pressure on dust. Soifer et al. (2003) noted that super star clusters (SSCs) can have a luminosity surface density at parsec scale as high as the Seyfert nuclei do at a few 10 pc scale. For example, the most luminous SSC in the dwarf galaxy NGC 5253 has age  $\sim 1$  Myr, FWHM size  $\sim 1$  pc, mass  $\sim 10^{5.5} M_{\odot}$  (Turner & Beck 2004; Calzetti et al. 2015), and hence luminosity  $\sim 10^{8.5} L_{\odot}$  and luminosity surface density  $\sim 10^{14.5} L_{\odot} \text{ kpc}^{-2}$ . The Arches cluster in the center of our Galaxy also has almost the same luminosity surface density (Lang et al. 2005). From this comparison, empirically speaking, a luminous AGN is a plausible source of luminosity for the central core  $W_1 \approx W_1'$  in the western nucleus. Obviously, an empirical argument cannot rule out the possibility that by far the most intense starburst in the local universe is at the center of Arp 220 W. Our new constraint for the case where star formation dominates the luminosity is that the starburst in the central 20 pc must be equivalent to several thousands of massive young SSCs. Tighter constraints on the luminosity source are expected from further ALMA observations. The center of Arp 220 W likely has a column density to make the 3 mm dust opacity on the order of unity and hence a mass surface density of  $\sim 10^6 M_{\odot} \text{ pc}^{-2}$  (S17; BM15). The central 20 pc of Arp 220 W is therefore at or above the Eddington limit for dust (Andrews & Thompson 2011; see Equation (7)). The bipolar outflow from Arp 220 W is therefore expected. The nucleus has been actively forming stars in the nuclear disk, feeding either a luminous AGN or exceptionally intense starburst at the center, and blowing out dust and gas at the same time. The nucleus is certainly in a phase of rapid evolution.

## 7. Conclusions

We analyzed ALMA high-resolution data of Arp 220 at  $\sim 3$  mm wavelengths. We spatially resolved the continuum structure of the individual nuclei and decomposed the nuclei into plasma and dust emission. The dust emission was then used to characterize the luminosity source in the western nucleus. Our major observations are the following.

1. Both nuclei are found to have at least two structural components at 3 mm. Two concentric components, such as Gaussians or a Gaussian and an exponential disk, provide reasonable fits to the observed visibilities.
2. The larger components in the two-Gaussian fit have FWHM sizes  $\sim 0''.23$ – $0''.37$  (100–150 pc) and axial ratios  $\sim 2$ . They match in shape and extent the distributions of the supernova features seen with VLBI. We identify them with the starburst nuclear disks rotating around the individual nuclei with inclinations  $\approx 60^{\circ}$ .
3. The smaller components in the two-Gaussian fit contribute about 20% and 50% of the 3 mm continuum flux densities of the eastern and western nuclei, respectively. They have FWHM sizes of 20–40 pc and peak brightness temperatures 70–640 K, which are more than twice smaller and brighter than those in the previous single-Gaussian fit of the same data.
4. The 3 mm continuum spectral slopes are flat ( $S_{\nu} \propto \nu^{0.0 \pm 0.2}$ ) and positive ( $\propto \nu^{1.2 \pm 0.2}$ ) at the eastern and western nuclei, respectively. Combining them with the 33 GHz data of the plasma emission, we estimate that dust emits about 13% and 41% of the 3 mm continuum in the eastern and western

nuclei, respectively. The dust emission is found centrally concentrated in both nuclei. These central cores of dust emission correspond to the compact components in our two-component fitting.

5. The dust-continuum core of the western nucleus is estimated to have a peak brightness temperature of  $\sim 530$  K and a major axis FWHM of about 20 pc after subtracting plasma emission. Assuming a dust disk, its bolometric luminosity can be as large as  $\sim 10^{12.5} L_{\odot}$  or at least a large fraction of the total luminosity of Arp 220. Its luminosity surface density is on the order of  $10^{15.5} L_{\odot} \text{ kpc}^{-2}$  in 20 pc scale. This is about an order of magnitude higher than observed toward some Seyfert nuclei at the same scale and SSCs at parsec scale. This comparison favors the presence of a luminous AGN on empirical grounds, but we stress the uncertainties that are still in the data interpretation, the inherent limitation of the empirical argument, and the need for further observational and theoretical constraints.
6. The western nucleus has a faint extended, linear feature along the projected minor axis of its nuclear disk; this is the third structural component for the nucleus. We attribute it to the previously inferred bipolar outflow.

We are grateful to the ALMA Observatory and its data archive team for the observations and data we used here. We thank the ALMA help desk for their prompt response to our numerous inquiries about ALMA observations and data reduction. We also thank our referee for comments that helped clarify this paper. This paper makes use of the following ALMA data: ADS/JAO.ALMA#2015.1.00113.S and ADS/JAO.ALMA#2011.0.00001.CAL. ALMA is a partnership of ESO (representing its member states), NSF (USA), and NINS (Japan), together with NRC (Canada), MOST and ASIAA (Taiwan), and KASI (Republic of Korea), in cooperation with the Republic of Chile. The Joint ALMA Observatory is operated by ESO, AUI/NRAO, and NAOJ. This research has made use of NASA's Astrophysics Data System Bibliographic Services. This research has also made use of the NASA/IPAC Extragalactic Database (NED), which is operated by the Jet Propulsion Laboratory, California Institute of Technology, under contract with the National Aeronautics and Space Administration. K.S. is supported by MOST grants 105-2119-M-001-036 and 106-2119-M-001-025.

Facility: ALMA.

Software: CASA v4.7.2 (McMullin et al. 2007), mpfit (Moré 1978; Moré & Wright 1993; Markwardt 2009).

## ORCID iDs

Kazushi Sakamoto  <https://orcid.org/0000-0001-5187-2288>

Loreto Barcos-Muñoz  <https://orcid.org/0000-0003-0057-8892>

Francesco Costagliola  <https://orcid.org/0000-0002-9155-5188>

Sergio Martín  <https://orcid.org/0000-0001-9281-2919>

David Wilner  <https://orcid.org/0000-0003-1526-7587>

## References

- Aladro, R., Martín, S., Riquelme, D., et al. 2015, *A&A*, 579, A101  
 Andrews, B. H., & Thompson, T. A. 2011, *ApJ*, 727, 97  
 Armus, L., Mazzarella, J. M., Evans, A. S., et al. 2009, *PASP*, 121, 559

- Barcos-Muñoz, L. 2016, PhD thesis, Univ. Virginia, [https://libra2.lib.virginia.edu/public\\_view/gt54kn02m](https://libra2.lib.virginia.edu/public_view/gt54kn02m)
- Barcos-Muñoz, L., Leroy, A. K., Evans, A. S., et al. 2015, *ApJ*, 799, 10
- Barcos-Muñoz, L., Leroy, A. K., Evans, A. S., et al. 2017, *ApJ*, 843, 117
- Batejat, F., Conway, J. E., Hurley, R., et al. 2011, *ApJ*, 740, 95
- Briggs, D. S. 1995, PhD thesis, New Mexico Institute of Mining and Technology, <http://www.aoc.nrao.edu/dissertations/dbriggs/>
- Calzetti, D., Johnson, K. E., Adamo, A., et al. 2015, *ApJ*, 811, 75
- Cicone, C., Maiolino, R., Sturm, E., et al. 2014, *A&A*, 562, A21
- Clements, D. L., Dunne, L., & Eales, S. 2010, *MNRAS*, 403, 274
- Downes, D., & Eckart, A. 2007, *A&A*, 468, L57
- Evans, A. S., Becklin, E. E., Scoville, N. Z., et al. 2003, *AJ*, 125, 2341
- Genzel, R., Tacconi, L. J., Rigopoulou, D., Lutz, D., & Tecza, M. 2001, *ApJ*, 563, 527
- González-Alfonso, E., Fischer, J., Bruderer, S., et al. 2013, *A&A*, 550, A25
- González-Alfonso, E., Fischer, J., Graciá-Carpio, J., et al. 2012, *A&A*, 541, A4
- Hopkins, P. F., Hernquist, L., Cox, T. J., & Kereš, D. 2008, *ApJS*, 175, 356
- Lang, C. C., Johnson, K. E., Goss, W. M., & Rodríguez, L. F. 2005, *AJ*, 130, 2185
- Lonsdale, C. J., Diamond, P. J., Thrall, H., Smith, H. E., & Lonsdale, C. J. 2006, *ApJ*, 647, 185
- Markwardt, C. B. 2009, in ASP Con. Ser. 441, *Astronomical Data Analysis Software and Systems XVIII*, ed. D. A. Bohlender et al. (San Francisco, CA: ASP), 251
- Martín, S., Aalto, S., Sakamoto, K., et al. 2016, *A&A*, 590, A25
- Martín, S., Krips, M., Martín-Pintado, J., et al. 2011, *A&A*, 527, A36
- Martí-Vidal, I., Pérez-Torres, M. A., & Lobanov, A. P. 2012, *A&A*, 541, A135
- McMullin, J. P., Waters, B., Schiebel, D., Young, W., & Golap, K. 2007, *adass XVI*, 376, 127
- Moré, J. 1978, in *Numerical Analysis*, Vol. 630, ed. G. A. Watson (Berlin: Springer), 105
- Moré, J., & Wright, S. 1993, *Optimization Software Guide*, Vol. 14 (Philadelphia: SIAM)
- Paggi, A., Fabbiano, G., Risaliti, G., et al. 2017, *ApJ*, 841, 44
- Parra, R., Conway, J. E., Diamond, P. J., et al. 2007, *ApJ*, 659, 314
- Planck Collaboration, Abergel, A., Ade, P. A. R., et al. 2011, *A&A*, 536, A21
- Rangwala, N., Maloney, P. R., Glenn, J., et al. 2011, *ApJ*, 743, 94
- Rovilos, E., Diamond, P. J., Lonsdale, C. J., Lonsdale, C. J., & Smith, H. E. 2003, *MNRAS*, 342, 373
- Sakamoto, K., Aalto, S., Combes, F., Evans, A., & Peck, A. 2014, *ApJ*, 797, 90
- Sakamoto, K., Aalto, S., Costagliola, F., et al. 2013, *ApJ*, 764, 42
- Sakamoto, K., Aalto, S., Wilner, D. J., et al. 2009, *ApJL*, 700, L104
- Sakamoto, K., Scoville, N. Z., Yun, M. S., et al. 1999, *ApJ*, 514, 68
- Sakamoto, K., Wang, J., Wiedner, M. C., et al. 2008, *ApJ*, 684, 957
- Sanders, D. B., & Mirabel, I. F. 1996, *ARA&A*, 34, 749
- Scoville, N., Murchikova, L., Walter, F., et al. 2017, *ApJ*, 836, 66
- Scoville, N., Sheth, K., Walter, F., et al. 2015, *ApJ*, 800, 70
- Scoville, N. Z., Evans, A. S., Dinshaw, N., et al. 1998, *ApJL*, 492, L107
- Seaquist, E. R., & Clark, J. 2001, *ApJ*, 552, 133
- Smith, H. E., Lonsdale, C. J., Lonsdale, C. J., & Diamond, P. J. 1998, *ApJL*, 493, L17
- Soifer, B. T., Bock, J. J., Marsh, K., et al. 2003, *AJ*, 126, 143
- Soifer, B. T., Neugebauer, G., Matthews, K., et al. 2001, *AJ*, 122, 1213
- Thompson, T. A., Quataert, E., & Murray, N. 2005, *ApJ*, 630, 167
- Tunnard, R., Greve, T. R., Garcia-Burillo, S., et al. 2015, *ApJ*, 800, 25
- Turner, J. L., & Beck, S. C. 2004, *ApJL*, 602, L85
- Varenus, E., Conway, J. E., Batejat, F., et al. 2017, [arXiv:1702.04772](https://arxiv.org/abs/1702.04772)
- Varenus, E., Conway, J. E., Martí-Vidal, I., et al. 2016, *A&A*, 593, A86
- Veilleux, S., Meléndez, M., Sturm, E., et al. 2013, *ApJ*, 776, 27
- Walter, F., Weiss, A., & Scoville, N. 2002, *ApJL*, 580, L21
- Wiedner, M. C., Wilson, C. D., Harrison, A., et al. 2002, *ApJ*, 581, 229
- Wilson, C. D., Rangwala, N., Glenn, J., et al. 2014, *ApJL*, 789, L36
- Yoast-Hull, T. M., Gallagher, J. S., Aalto, S., & Varenus, E. 2017, *MNRAS*, 469, 89
- Zschaechner, L. K., Ott, J., Walter, F., et al. 2016, *ApJ*, 833, 41